12th AIAA/CEAS Aeroacoustics Conference (27th AIAA Aeroacoustics Conference)
8 - 10 May 2006, Cambridge, Massachusetts

AIAA 2006-2555

Numerical Study of Aeroacoustic Oscillations in Transonic Flow Downstream a Sudden Duct Enlargement

Thomas Emmert * and Philippe Lafon ††

Laboratoire de Mécanique des Structures Industrielles Durables,
UMR CNRS EDF 2823, Clamart, France

Christophe Bailly ‡

Laboratoire de Mécanique des Fluides et d'Acoustique,
École Centrale de Lyon & UMR CNRS 5509, Ecully, France

A sonic flow passing a sudden enlargement in a plane duct is numerically studied by solving the 2-D compressible Navier-Stokes equations. Different flow patterns are likely to appear in such configuration. For very low pressure ratios the flow is entirely supersonic and stable. For higher ratios, unstable flow patterns emerge. One of these patterns features a normal shock, that oscillates due to a self-exciting mechanism. As the duct is open at the outflow, aeroacoustics coupling occurs when the shock oscillations get in resonance with the longitudinal acoustic modes of the duct. The main flow features are captured by the present numerical simulations but no coupling with longitudinal duct modes is found because of 2-D artefacts. The governing equations are solved using high-order methods based on central finite differences on structured grids. To damp out spurious oscillations supported by central differences a selective background smoothing term and a well established non-linear shock-capturing term are used. Their suitability is demonstrated by two test cases involving a classical shock-sound interaction problem and an abruptly expanding supersonic inviscid flow.

I. Introduction

Strong interactions between shock oscillations, internal aerodynamic noise and longitudinal duct modes are often observed in confined flows but are undesirable to prevent excitation of structural vibrations and fatigue. Numerous examples can be found in the nice review of Meier *et al.*[1]

A transonic flow passing a sudden expansion in a duct is a classical flow configuration encountered in pipe systems of power plants. This flow can be found downstream of control devices such as valves and has been investigated experimentally by Meier *et al.*[2] These authors studied a transonic flow in a rectangular duct displayed in Figure 1 for different expansion ratios $\tau = p_e/p_a$. For very low ratios the flow in the upstream part of the test duct is entirely supersonic. A system of steady oblique shock waves then occurs when the expansion waves that are generated at the inlet angles are reflected by the upper and lower walls. Increasing the exit pressure leads to a flow separation and to a breakdown of the shock cell structure. Shock pattern oscillations are then observed. If the downstream pressure is further increased, the oblique shock wave system disappears and the supersonic expansion ends up after a single normal shock. In this case, a strong coupling between the oscillations of the normal shock and the longitudinal acoustic modes of the duct is found. Meier *et al.*[2] provide time sequence visualizations of the different flow regimes based on Mach-Zehnder Interferometry. Static wall pressure data, frequency spectra and cross correlations of the

*PhD student.
†Research engineer, AIAA member
‡Professor, AIAA member.

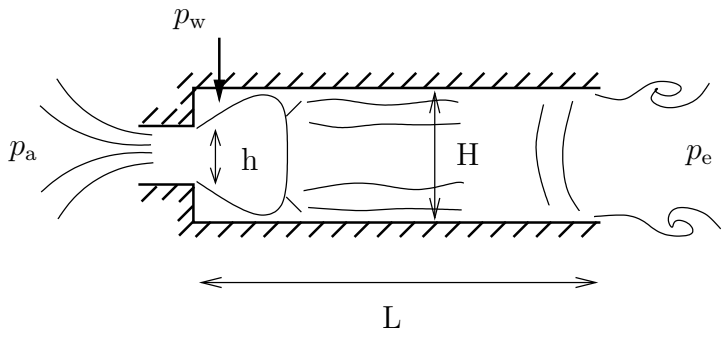

Figure 1. Sketch of the studied geometry : $L = 0.160$ **m,** $\mathbf{L/H} = 4.82$ **and** $\mathbf{h/H} = 0.3$**.**

pressure fluctuations along the walls are also available, making possible a quantitative validation of numerical simulations.

Devos and Lafon[3] have studied numerically the same configuration, using a second-order TVD finite-volume scheme for solving 2-D Euler equations. The main flow patterns were captured, but the coupling of the shock oscillations with the resonance modes of the duct was not considered.

In the present work a new numerical algorithm is developed to simulate aeroacoustic couplings for internal flows in complex geometries. High-order schemes are used to preserve the generated acoustic field and a non-linear adaptive filter is implemented to capture strong shock waves. The viscous effects play a key role for the reattachement or not of the flow. The compressible Navier-Stokes equations are therefore solved in the present work.

The paper is organized as follows. The numerical algorithm is briefly discussed in section II. Two test cases are reported in section III as validation. Results of a simulation of the experiments by Meier *et al.*[2] and comparisons with measurements are presented in section IV. Then, concluding remarks are given in section V.

II. Governing equations and numerical algorithm

The set of equations are the 2-D Navier-Stokes equations, written in conservative form after application of a general time-invariant curvilinear coordinate transformation $(x, y) \rightarrow (\xi, \eta)$ as:

$$\frac{\partial}{\partial t}\Big(\frac{\mathbf{Q}}{J}\Big) + \frac{\partial \mathbf{E}}{\partial \xi} + \frac{\partial \mathbf{F}}{\partial \eta} = 0.$$

The solution vector in the above equation is given by $\mathbf{Q} = (\rho, \rho u, \rho v, \rho e)^T$. The flux vectors **E**,**F** contain the inviscid and the viscous terms. Their expressions as well as the metric identities for the grid transformation can be found in the work of Visbal and Gaitonde or Marsden *et al.*[4,5] The viscosity is determined by Sutherland's law:

$$\nu(T) = \nu_0 \sqrt{\frac{T}{T_0}} \frac{1 + \frac{C}{T_0}}{1 + \frac{C}{T}}$$

where $T_0 = 273$ K is the ambient temperature. The fluid dependent parameters for air are $\nu_0 = \nu(T_0) = 1.5 \times 10^{-5}$ m^2.s^{-1} and $C = 110$ K.

For interior points of the computational domain, the fluxes and the velocity derivatives for the viscous terms are discretized by a centered 11-point finite difference scheme developed by Bogey and Bailly.[6] This scheme has been optimized in wave number space and is able to resolve accurately perturbations with only four points per wavelength. An appropriate explicit 11-point low pass filter remove grid-to-grid oscillations, not resolved by centered finite difference schemes. The filtering coefficient is chosen to be 0.2 inside the computational domain.

In order to preserve accuracy near the wall boundaries the optimized 11-points off centered finite difference schemes such as developed by Berland *et al.*[7] are used. Unfortunately the associated non centered filters exhibit stability problems, when the mesh is stretched or contains discontinuities. Therefore the following

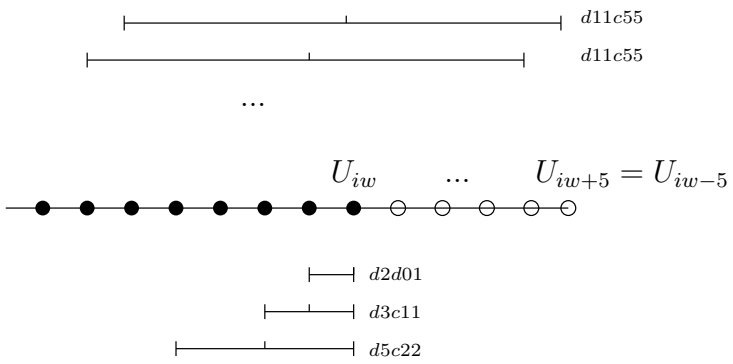

Figure 2. Application of selective filters at wall points: dK(c/d)LM denotes a K-points centered/non-centered filter that involves L points to its left and M points to its right; • are interior points; ∘ are ghost points.

two-step strategy has been adopted. First the centered 11-point filter is applied at all boundary points. The unknown values at the ghost points outside the computational domain are updated by the values of the mirror points as illustrated in Figure 2. Second the last three boundary points need to be stabilized by low-order centered filters of fourth-, second- and first order respectively. This filtering strategy is sufficient to ensure numerical stability in smooth regions.

In regions with strong shocks, additional numerical dissipation is introduced by using the adaptive non-linear artificial dissipation model of Kim and Lee.[8] In the present computations the second-order filter for cartesian coordinates is used. It yields:

$$\mathbf{Q}_i^{n+1} = \hat{\mathbf{Q}}_i^{n+1} - (\mathbf{D}_{i+\frac{1}{2}} - \mathbf{D}_{i-\frac{1}{2}}),$$

where

$$\mathbf{D}_{i+\frac{1}{2}} = \frac{\Delta|\lambda|_{i+\frac{1}{2}}^{\text{stencil}}}{\Delta x}\ \epsilon_{i+\frac{1}{2}}^{(2)}\ \Delta t\big(\hat{\mathbf{Q}}_{i+1} - \hat{\mathbf{Q}}_i\big).$$

$\hat{\mathbf{Q}}$ is the solution vector that has already been treated by the linear selective filter. The quantity $\Delta|\lambda|_{i+\frac{1}{2}}^{\text{stencil}}$ denotes the difference between the greatest and the smallest eigenvalue $|\lambda|_i = (|u| + c)_i$ within a stencil of variable size. According to Kim and Lee a stencil width of 7 points is chosen:

$$\Delta|\lambda|_{i+\frac{1}{2}}^{\text{stencil}} = \max_{m=-2}^{3}\ (|\lambda|_{i+m}) - \min_{m=-2}^{3}\ (|\lambda|_{i+m}).$$

Note that the damping term reduces to first-order when $\Delta|\lambda|_k^{\text{stencil}}\epsilon_k^{(2)}$ takes different values for $k = i + \frac{1}{2} = i - \frac{1}{2}$, which is only the case for strong shocks. The artificial dissipation is more important for wider stencils and can be tuned by varying its size in order to find the most suitable relation between accuracy and stability. The centered character of the selective and non-linear filters ensure no dispersion error unless the non-linear filter reduces to first-order. Both filters are applied once after every time integration cycle in each coordinate direction separately. This keeps the computational effort for the non-linear filter as low as possible.

In order to ensure a high-quality solution, the second-order filter may only be applied locally in the shock region. This is performed by the adaptive non-linear function $\epsilon_{i+\frac{1}{2}}^{(2)}$ that reaches its maximum in regions of strong shocks and is very small in smooth regions. The shock position is detected by using the curvature of the pressure. For further details about the detection procedure and about the extension to curvilinear geometries refer to the work of Kim and Lee.[8]

A fourth-order low-storage Runge Kutta scheme advances the solution in time. The standard Message Passing Interface (MPI) library routines have been used for the code parallelization.

III. Two test cases as validation

In this section two test cases are presented. The first one deals with the acoustic propagation in a transonic convergent divergent nozzle. The second one is devoted to a steady supersonic flow in a sudden

duct expansion. Note that all the numerical results of this section are obtained with the Euler equations.

A. Convergent divergent nozzle

The first test case presented here, was proposed by the first ICASE-NASA benchmark workshop.[9] The influence of the non-linear filter on the acoustic field is reported and an error estimate is performed. The governing equations are the 1-D Euler equations with varying cross section $A(x)$ and are solved in conservative form such as:

$$\frac{\partial(A\mathbf{Q})}{\partial t} + \frac{\partial(A\mathbf{E})}{\partial x} - \mathbf{H} = 0,$$

where $\mathbf{Q} = [\rho, \rho u, \rho e]^T$, $\mathbf{E} = [\rho u, \rho u^2 + p, (\rho e + p)u]^T$ and $\mathbf{H} = [0, p\ \mathrm{d}A/\mathrm{d}x, 0]^T$. The total specific energy e is defined as $e = p/(\gamma - 1)/\rho + 0.5\ u^2$. The properties ρ, u, p are non dimensionalized by ρ_0, c_0 and $\rho_0 c_0^2$ respectively.

The cross section area $A(x)$ for the convergent divergent nozzle is given by:

$$A(x) = \begin{cases} 134 & x \leq -100 \\ 117 - 17\cos(\frac{\pi x}{100}) & -100 \leq x \leq 19 \\ 97.2 + 0.3x & 19 \leq x \leq 80. \end{cases}$$

Note that the first derivative of $A(x)$ features two discontinuities at $x = -100$ and $x = 19$ that generate spurious oscillations slowing down the local convergence of the mean flow field. Selective filtering eliminates these oscillations so that they do not mask the acoustical field.

The equations are solved on a uniform grid and the solution is advanced in time with CFL=0.4. At the inflow, a subsonic flow is imposed ($M_{in} = 0.5$, $\rho_{in} = 1$, $p_{in} = 1/\gamma$). Due to the low pressure ($p_{out} \approx 0.6363$) that is fixed at the outflow, the flow becomes transonic in the divergent part of the nozzle. The flow gets shocked at $x \approx 40$ as shown in Figure 3 (a).

The simulation is carried out first using the 11-points finite difference scheme with the selective filter only on a grid that contains 281 points. Overshoots around the discontinuities are observed. They are associated with the classical Gibbs phenomenon, which is typical for high-order methods.

Once the mean field is converged after 58000 iterations, a harmonic acoustic perturbation (10^{-6} order of magnitude, $\omega = 0.1\pi$) is superimposed at the inflow in order to study shock-sound interaction. Figure 4 (a) displays the fluctuating pressure field. The ratio $\frac{p_2'}{p_1'}$ of amplitudes for the acoustic waves just in front and just behind the shock corresponds well to the first-order approximation given by Landau and Lifchitz:[10]

$$\frac{p_2'}{p_1'} = \frac{(1 + M_1)^2}{1 + 2M_2 + 1/M_1^2}\left[1 - \frac{\gamma - 1}{\gamma + 1}(1 - \frac{1}{M_1^2})^2\right].$$

The same simulation is repeated in combination with the non-linear filter. The local introduction of a second-order filter makes the solution converging twice as fast as without (*i.e.* after about 20000 iterations). Figure 3 (b) displays the mean flow field, showing excellent shock capturing properties. Due to the local dissipation, the shock enlarges slightly and nearly no oscillations are generated around the shock.

In order to check the influence of the non-linear filter on the acoustic field, the pressure signal at the outflow is recorded. In Figure 5 (a) the signals obtained with and without the non-linear filter are plotted against the nondimensionalized time. The two signals seem to be superposed. Assuming that the signal obtained without the non-linear filter is the reference solution, Figure 5 (b) displays the relative error of the signal obtained with non-linear filtering. As the lower curve reveals, the error remains under 1.5 % for waves resolved by 30 points per wave length. A further simulation is done on a coarser grid containing 141 points. In order to mask the error of the time integration, the same time step Δt as before is used. The signal is more damped when it passes the shock. The error estimate displayed in Figure 5 (b) shows that for waves resolved by 15 points per wave length the amplitude error remains under 4%.

B. Steady supersonic flow in a sudden duct expansion

In this section the supersonic flow downstream a sudden duct expansion given in Figure 1 is studied by neglecting viscous effects and thermal conduction. This is a preliminary computation of the work reported in section IV.

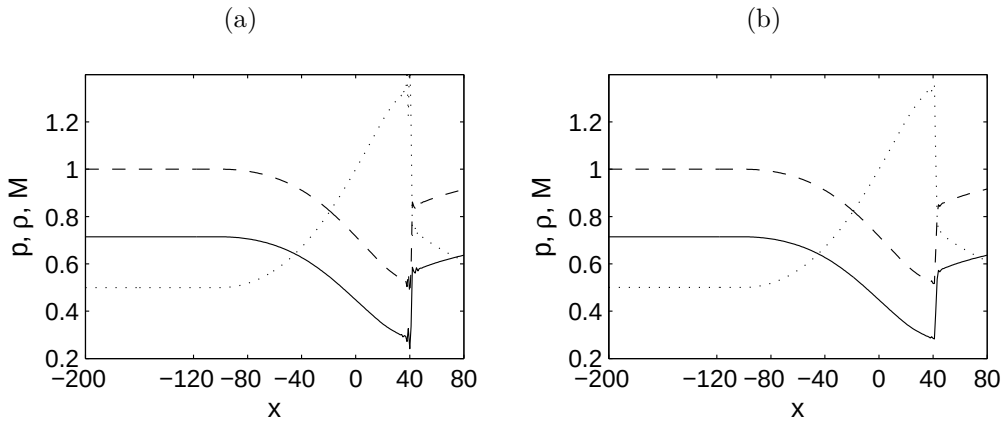

Figure 3. Mean profile ——— p, – – – ρ, ····· M: (a) with 11-points finite difference scheme only; (b) with 11-points finite difference scheme and non-linear filter.

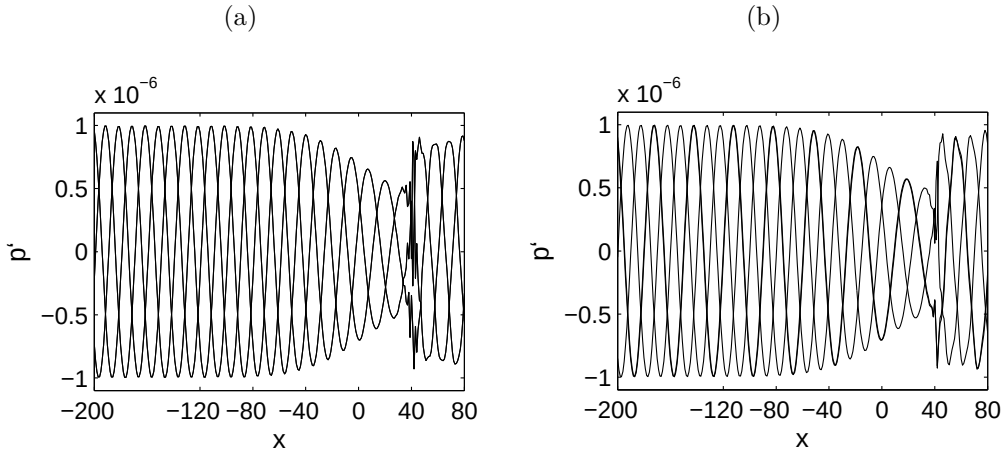

Figure 4. Pressure fluctuations field: (a) with 11-points finite difference scheme only; (b) with 11-points finite difference scheme and non-linear filter.

1. Simulation parameters

The grid of the duct contains $N_x \times N_y = 255 \times 132$ points. The grid spacing in x-direction $\Delta x = 2.64 \times 10^{-4}$ m near the nozzle is increased smoothly using a tangent hyperbolic function up to 7×10^{-4} m in the first quarter of the duct and remains constant up to the duct end. The grid in y-direction is uniform with $\Delta y = 2.64 \times 10^{-4}$ m. The outflow reservoir contains $N_x \times N_y = 80 \times 250$ points. The grid is stretched in x- and y-direction with 2%. The non-reflecting boundary conditions of Tam and Dong[11] are applied along the reservoir boundaries. A Laplacian filter is applied on the last 25 points at the downstream reservoir boundary in order to damp out strong perturbations before reaching the reservoir boundaries. The nozzle consists of $N_x \times N_y = 5 \times 44$ points in order to apply the interior 11-points finite difference scheme at the duct inlet. At all wall boundaries slip conditions are applied.

The upstream pressure $p_a = 101325$ Pa and temperature $T_a = 293$ K are chosen according to the experimental conditions. In order to obtain a supersonic flow in the whole duct, the pressure ratio is $\tau = 0.17$ giving the downstream pressure of $p_e = 17225$ Pa. At the nozzle a uniform sonic flow is imposed such as:

$$M_{in} = u_{in}/c_{in} = 1.01,\ v_{in} = 0,\ p_{in} = 0.5221\ p_a,\ T_{in} = 0.8306\ T_a.$$

where p_{in} and T_{in} are calculated from tables for isentropic 1-D flow in a duct with variable cross-section.

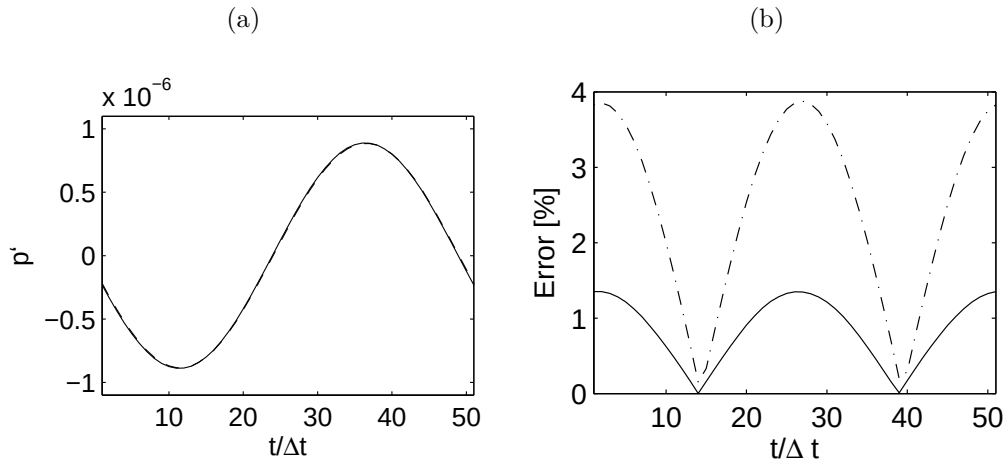

Figure 5. (a) Time evolution of fluctuating pressure field at the outflow $x = 80$: ——— with 11-points finite difference scheme only, – – – with 11-points finite difference scheme and non-linear filter; (b) Relative error at outflow: ——— with 281 points grid, with 141 points grid.

A number of 50000 iterations are performed on a single processor Intel Xeon 2800 MHz by using a CFL number of 0.9. The computation is stopped when the mean flow field does not change significantly.

2. Results

The plot of density iso-contours in Figure 6 (a) illustrates the numerical results. Qualitatively the results correspond well to the experiments presented in Figure 6 (b). A divergent supersonic jet formed by the expansion waves generated at the nozzle edges is observed. The first oblique shock wave appears when the expansion waves are reflected by the upper and lower wall. Further downstream the shock waves are reflected on the lower and upper wall respectively and form a symmetrical cell structure. As viscosity is removed no boundary layer develops. The oblique shock waves are reflected directly on the wall. In effect the shock waves interact with the flow boundary layer and are reflected in form of a system of compression and expansion waves, where in addition flow separation occurs as illustrated in Figure 6 (b). The shock waves are reflected distant from the wall so that the length of the cells in axial direction is smaller.

A more quantitative comparison is provided in Figure 8 (a) that displays the computed and measured static pressure along the walls. Note that the experimental curve is a fit of measured points. As there are not enough pressure sensors, only smooth regions are sufficiently resolved. In those regions simulation and experiment fit well. However the reattachement of the expanding supersonic jet is located too far upstream. One can state that the maximum pressure is predicted too high whereas the pressure in the base region p_w is too low, even if there are not enough pressure sensors allowing to reconstruct the measured pressure distribution. This is caused by a strong recirculation zone that can be observed in the dead air regions and reaches even supersonic speeds, as Figure 7 illustrates. This strong recirculation decreases the pressure seriously and makes the jet to reattache further upstream as in reality. This is due to the absence of viscosity and of 3-D mixing as a 2-D artefact. At the downstream end of the duct from $x = 0.12$ to $x = 0.16$, an insufficient number of pressure sensors makes a reliable validation impossible.

The pressure profile along $y = 0$ is plotted in Figure 8 (b). The shocks are well captured and their shock profiles are very sharp. Around the first shock at $x = 0.045$, nearly no oscillations can be observed in the pressure and density profiles. Around the second shock located at $x = 0.11$ small oscillations occur. These overshoots are associated to the Gibbs phenomenon which are typical for high-order methods. This indicates that the non-linear low-order filter is less dominant as the stencil eigenvalue $\Delta|\lambda|^{\text{stencil}}_{i+\frac{1}{2}}$ in this region is smaller.

(a)

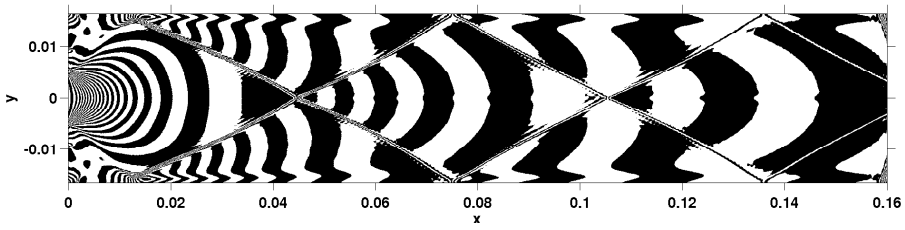

(b)

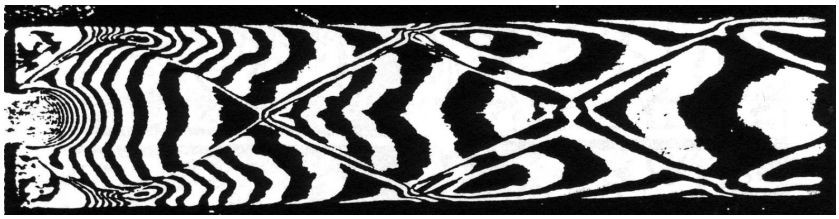

Figure 6. Iso-density contours $p_e/p_a = 0.17$ (a) present simulation, (b) experiments[2] obtained by Mach-Zehnder Interferometry.

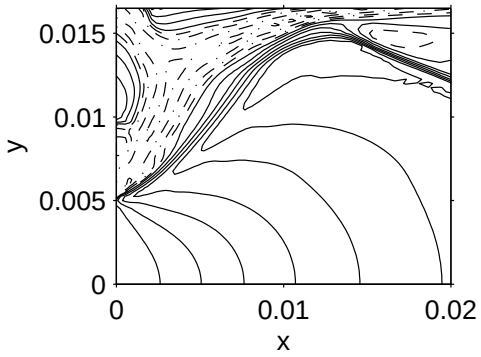

Figure 7. Mach iso-contours: solid lines for $M > 1$, dashed lines for $M < 1$.

IV. Transonic flow downstream a sudden duct enlargement

In this section the transonic flow downstream an abrupt expansion is simulated by solving the 2-D compressible Navier-Stokes equations. The sketch of the geometry is given in Figure 1. The pressure ratio is taken to be $\tau = p_e/p_a = 0.348$ following the experiments of Meier *et al.*[2] For this configuration a strong aeroacoustic coupling is observed by these authors.

A. Simulation parameters

The computational domain is decomposed in three sub-domains. First, the nozzle that contains $N_x \times N_y = 100 \times 90$ points. In x-direction the grid reaches its minimum mesh size $\Delta x = 5 \times 10^{-5}$ m at the nozzle outflow. Further upstream, the nozzle grid is stretched with a ratio of 1.5%. In y-direction the grid size is reduced near the walls from $\Delta y = 10 \times 10^{-5}$ m at the duct centerline down to $\Delta y = 5 \times 10^{-5}$ m using a smooth hyperbolic tangent function. Second, the duct is discretized with $N_x = 483$ points along the x- and $N_y = 324$ points along the y-direction. The grid size in x-direction is stretched by a hyperbolic tangent function from $\Delta x = 5 \times 10^{-5}$ m at the nozzle to $\Delta x = 20 \times 10^{-5}$ m in the middle of the duct. The grid size is reduced down to $\Delta x = 10 \times 10^{-5}$ m at the downstream end of the duct. As for the nozzle the grid size in y is reduced near the walls down to $\Delta y = 1 \times 10^{-5}$ m. Third, the outflow reservoir contains $N_x \times N_y = 200 \times 680$ grid points. The grid is stretched in x- and y- direction 20 points away from the duct outflow by a ratio of 1.5%. Another 40 points further away the grid is stretched with 3%. The last 30 points in x-direction of the

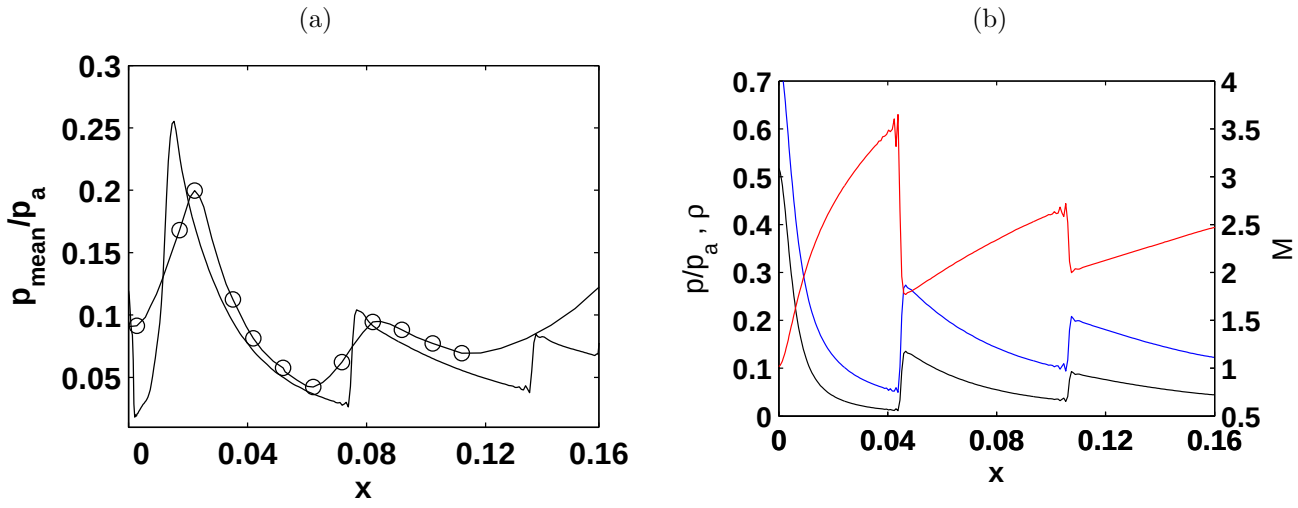

Figure 8. (a) Static pressure distribution along the duct wall, obtained by the present computation and experiments[2] (○ indicates the pressure sensor positions); (b) ——— p/p_a, ——— ρ, ——— M along the line $y = 0$ obtained by the present computation.

reservoir grid are highly stretched with 4% and are used for a sponge zone. The computation of the reservoir is necessary in order to ensure the acoustical properties of the open duct in spite of high computational costs. The flow is highly unsteady at the duct outflow which makes the application of numerical boundary conditions unsuitable.

The CFL number is 0.9 and the time step Δt is updated every iteration during the transient phase. Around 5×10^5 iterations has to be run in order to obtain an appropriate resolution on the low frequency components. The solver is performed on a cluster of five AMD Opteron 248 2200 MHz processors that are connected by a Gbit ethernet. The time for one Runge Kutta cycle is 0.945 s

B. Boundary Conditions

Similarly to the validation test case in section III.B, the nozzle is connected to ambient air which imposes a constant pressure $p_a = 101325$ Pa and constant temperature of $T_a = 293$ K. The appropriate inflow conditions are the same as in section III.B.

The velocity profile in the nozzle is kept uniform since slip wall conditions are applied. This approximation is justified as the nozzle length is short and the developing boundary layer is expected to be very thin and transitional. The Reynolds number based on the nozzle height and the inflow velocity is 2.1×10^5.

It was supposed that the air in the downstream reservoir and the ambient air are at rest and in thermodynamic equilibrium which gives $T_e = T_a$. Along the reservoir boundaries, the radiation condition of Tam and Dong[11] is applied. In order to avoid numerical drift and to maintain the pressure ratio $\tau = 0.348$, the downstream mean pressure $p_e = 35260$and density $\rho_e = \rho_e(p_e, T_e)$ are recalled after each Runge-Kutta cycle at the boundaries of the downstream reservoir. To minimize reflections as low as possible the recall coefficient is chosen to be 5×10^{-3}. In the sponge zone, a Laplacian filter is applied in order to dissipate vortices before they reach the end of the computational domain and generate spurious acoustical perturbations.

C. Self-exciting shock oscillations

Figure 9 shows the instantaneous pressure fluctuation field of the entire computational domain. The acoustic waves that originate at the outflow of the test duct leave the computational domain without spurious reflections. Spots of pressure peaks exhausted at the test duct end indicate too large vortices that are typical for 2-D flows. They are dissipated by the sponge zone without generating spurious parasite waves. Thus the sponge layer is well suited. However the mean pressure in the reservoir $p_0 \approx 33400$ Pa could not be matched during the simulation and differs from the target value with an error of 6%. This indicates that the pressure

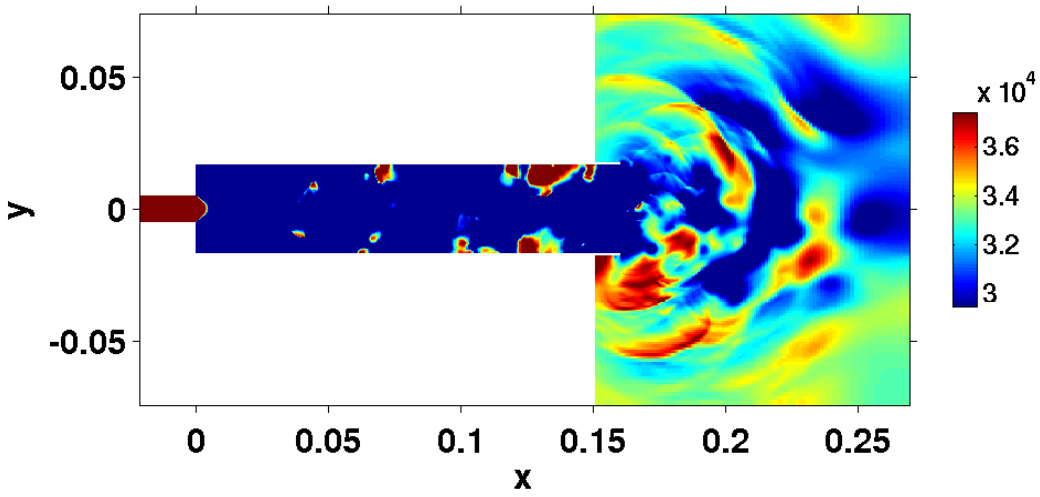

Figure 9. Instantenous pressure fluctuation field in [Pa].

reservoir is too small. Therefore new computations are currently done using a bigger reservoir where the mean pressure matches better with the target value.

Figures 10 (a) and (b) show the iso-density contours of the transonic flow that were obtained by computations for a duct of $L = 0.16$ m and by Mach-Zehnder Interferometry for a duct of $L = 0.24$ m respectively. A snapshot of the flow is reported when the base pressure p_w reaches its maximum. In both Figures, a normal shock with lambda feet at the extremities can be observed. Supersonic layers are formed further downstream of the lambda shocks. The computed shock is located too far downstream at $x = 0.04$ m with an error of 12.5%.

The corresponding computed and measured static pressure distributions along the upper and lower duct walls are given in Figure 10 (c). The computed pressure was averaged over 1000 frames which corresponds to 1×10^{-4} s. This averaging time was chosen arbitrarily as no time constant of the static pressure sensors is given by the experimenters. Only qualitative comparison is possible as the computed and the measured duct are of different length. Furthermore the reliability of the measurements were put into question by Meier *et al.*[2] as they observed transverse components of the flow in the static pressure holes.

In the experiment and at this expansion rate, the flow stays symmetric with respect to $y = 0$ during the whole oscillation cycle. The measured static pressure distributions as given in Figure 10 (c) are identical for the upper and the lower wall. The computed flow is more asymmetrical and the measured static pressure at the upper and the lower wall differ significantly as Figure 10 (c) illustrates. This asymmetrical character of the flow is a 2-D artefact. In 3-D the pressure on the lower and upper wall is equalized by the lateral walls and the jet remains stable in a symmetrical position.

The static pressure at the beginning of the upper base region ($x = 0$) fits well with the experimental pressure curve. The pressure in this region must be well predicted since it determines the flow regime downstream in the duct. Further upstream at $x = 0.04$ m the computed pressure has a small maximum indicating the region of the normal shock. The measured curve features a much more dominant pressure peak. In the lower base region, the pressure is much more lower and reaches a level comparable to the entire supersonic case (Figure 8 (a)). The pressure increases rapidly when the jet reattaches on the lower wall and the reflected expansion waves generate an oblique shock wave. Further downstream the static pressure on the upper and the lower duct converge to a value that is close to the downstream pressure p_e.

Figure 11 shows the instantaneous filter strength $\Delta|\lambda|^{\text{stencil}}_{i+\frac{1}{2}}\ \epsilon^{(2)}_{i+\frac{1}{2}}$ for the adaptive non-linear filter in x-direction that was computed for the instant represented in Figure 10 (a). The filter strength reaches its maximum at the normal shock and in some strongly non-linear regions further downstream. In regions with smooth gradients the filter strength is very low and in the outflow reservoir the filter strength is zero. This demonstrates the suitability of this filter for this kind of flows.

In the following, the computed self-exciting mechanism of the base pressure oscillations is explained. For that a sequence of the instantaneous u-velocity field and the instantaneous pressure field are given in Figure

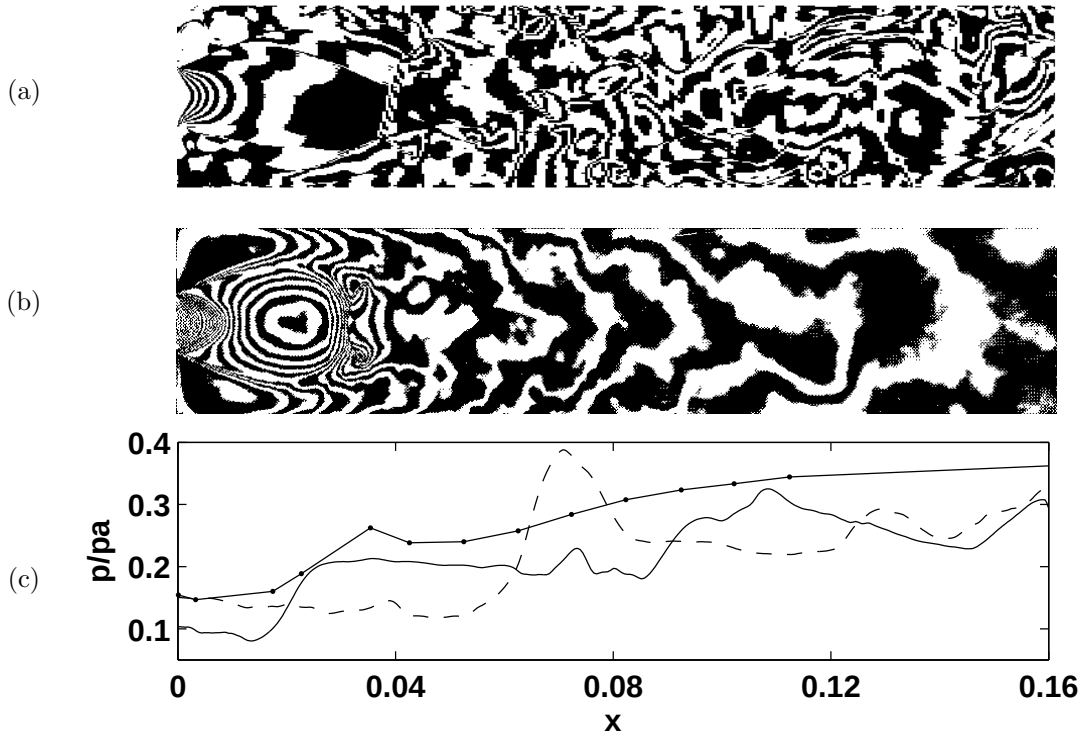

Figure 10. Iso-density contours (a) by present simulation. (b) by experiments[2] (Mach-Zehnder Interferometry) ; (c) Static pressure distribution along the upper and lower duct wall obtained by computation: ——— lower wall — — — upper wall; by experiments where • indicates the position of the pressure sensors.

12 (a) and (b) respectively.

Frame 1 shows the expanding jet that reattaches at the upper and at the lower walls. The jet ends up with a strong normal shock. Downstream of the extremeties, supersonic layers are formed that are separated from the duct walls and that reattach further downstream in the duct. A pressure rise downstream of the reattachment zone makes the jet to completely separate from the upper duct wall and a back flow from the reattachement region to the base region occurs (Frame 2-4). The backflow causes a pressure rise in the base region and the expansion angle of the jet becomes smaller. The height of the normal shock reduces (frames 4-7) and the pressure behind the shock decreases. The shock moves downstream and the flow becomes more "jet-like" with higher velocities in the flow core downstream of the shock (frames 5-8). The jet reaches its minimum expansion angle between frame 5 and 6. In frame 7, one observes an entrainment of flow from the base pressure region through the slit between the upper boundary layer and the supersonic jet which is due to a lower pressure in the post shock region. This leads to a further drop of the base pressure and is therefore a self-amplifying process. The expansion angle of the jet increases and the normal shock is moving upstream and reaches a position closer to the nozzle. As the shock strength increases, the pressure increases in post shock region. The boundary layer is disturbed by this pressure rise. The jet separates again of the wall: the loop is closed.

This mechanism is more obvious for the upper part of the duct but small pressure oscillations can also be observed in the lower base region. During one whole simulation the situation can inverse and stronger oscillations are observed on the lower duct wall. This wall switching is of random nature.

D. Aeroacoustic coupling

The self-exciting mechanism such as explained in the previous section exists without a coupled resonator. In this case the pressure oscillations are irregular. In the case considered here the open ended duct acts like a resonator. Meier *et al.*[1] describe the coupling as follows. When air is entrained by the supersonic jet, the static pressure decreases and the jet begins to expand (frame 6). The fall of the base pressure from

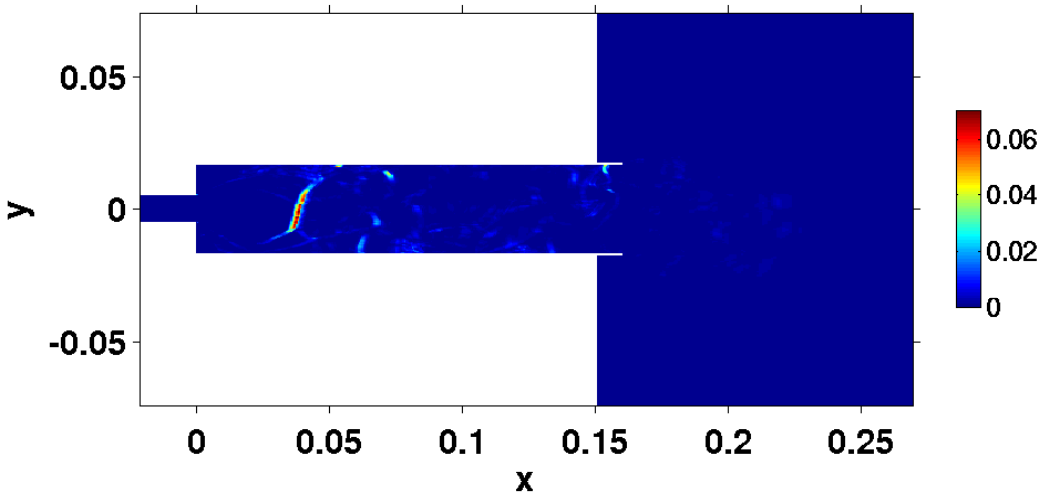

Figure 11. Instantenous strength of non-linear filter $\Delta|\lambda|^{\mathbf{stencil}}_{i+\frac{1}{2}}\ \epsilon^{(2)}_{i+\frac{1}{2}}$ in x-direction.

its equilibrium level diminishes the static pressure in the duct and leads to a deceleration of the flow. By equlibrium level Meier *et al.*[1] mean that level that securs a steady flow which fulfils mass, momentum and energy conservation along the duct. The emerging pressure difference at the duct end will produce in a subsonic flow a compression wave which decelerates the flow and pushes the shock into an extreme position towards the nozzle (frame 9). The pressure rise would make to separate the boundary layer and the normal shock of the jet would break down. Strong pressure oscillation can be measured in the whole duct. Meier *et al.*[2] found for the configuration considered in this paper a frequency of $f_{\text{exp}} = 373$ Hz.

Unfortunately no such a coupling could be reproduced numerically up to now. The oscillations described above were of irregular nature as the pressure signal recorded at $x = H/2$ in Figure 13 (a) shows. Figure 13 (b) gives the pressure signal further downstream at $x = 2H$ and demonstrates that no coupling takes place in the duct as the pressure signal is disturbed by random noise.

This coupling takes place only when the oscillation frequency of the shock is close to the resonant longitudinal duct frequencies. The resonant frequencies of the longitudinal modes can be estimated by the expression

$$f_{\text{duct},n} = (2n-1)(1-M^2)\ \frac{c}{4L}, \quad \text{for } n = 1, 2, 3 \ \text{ etc.} \tag{1}$$

This expression gives the frequencies of $(2n-1)\times$ quarter standing waves which are supported by a duct that is closed at one end ($u' = 0$) and that is open at the other end ($p' = 0$). The term $(1-M^2)$ takes into account the mean Mach number M of the subsonic flow behind the normal shock. The mean sound speed of the flow is denoted by c. Note that the upstream part of the duct can be treated as a closed end because a sonic flow is present at the throat at all times and no information can travel upstream through the nozzle.

Meier *et al.*[2] estimated the Mach number by a 1-D approach that can be found in the work of Jungowski.[12] The speed of sound are determined from tables of adiabatic flow. In the present paper the resonant frequency of the first longitudinal duct mode ($n = 1$) according to equation (1) is $f_{\text{duct},1} = 240$ Hz and for the second mode $n = 2$, $f_{\text{duct},2} = 744$ Hz. The values of $M = 0.68$ and $c = 295$ m/s are computed from the mean Mach number and mean sound velocity field in the post shock region. A base pressure cycle takes about 1.6×10^{-3} s according to Figure 13 (a) giving a shock oscillation frequency of $f_{S.O.} = 625$ Hz and does not match with neither the first nor the second duct mode.

Equation (1) identifies, beside the duct length, the Mach number and the speed of sound as determing parameter of the duct resonance. This requires the flow field to be reproduced as realistic as possible. The absence of lateral wall makes the flow asymmetrical and the normal shocks gets slightly oblique as the mean Mach number field in Figure 14 shows. The shocks get less strong and the Mach number behind the shock is predicted too high whereas the sound speed velocity is computed too low. This leads to lower frequencies according to equation (1). Therefore the next step will be to extend the 2-D solver to 3-D geometries.

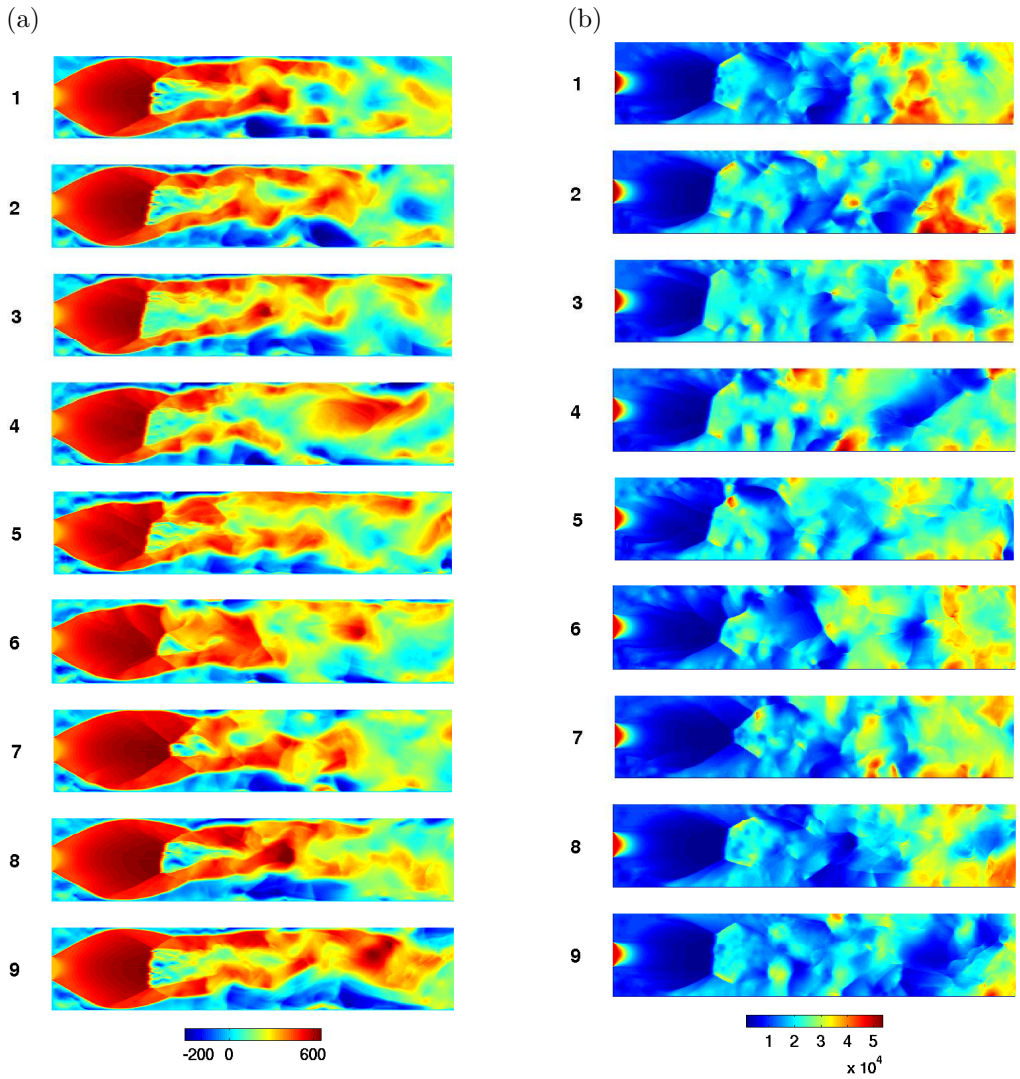

Figure 12. Time sequence of shock oscillation: (a) velocity component u [m/s], (b) Pressure p [Pa].

V. Concluding remarks

In this paper a numerical algorithm is proposed to deal with transonic and supersonic flows. An optimized finite difference scheme with low numerical dispersion and dissipation is combined with a selective high-order and a non-linear low-order filter that is introduced only in the shock region. Demonstrated by two validation test cases, the non-linear filter has good shock capturing properties and ensures a stable numerical solution of the suddenly expanded supersonic flow. In the unsteady transonic case, the algorithm is able to reproduce the complex self-exciting mechanism of the shock-oscillations by solving the compressible Navier-Stokes equations.

Because of 2-D effects, the self-excited oscillations of the normal shock are asymmetrical which affect the resonant properties of the duct. No aeroacoustic coupling can be observed. Therefore the extension of the solver for 3-D Navier-Stokes equations is in progress.

References

[1]Meier G.E.A., Szumowski A.P. and Selerowicz W.C. *Self-excited oscillations in internal transonic flows.* Progress in Aerospace Sciences, **2** (1990), 145-200.

[2]Meier G.E.A., Grabitz G., Jungowski W.M., Witczak K.J and Anderson J.S. *Oscillations of the supersonic flow*

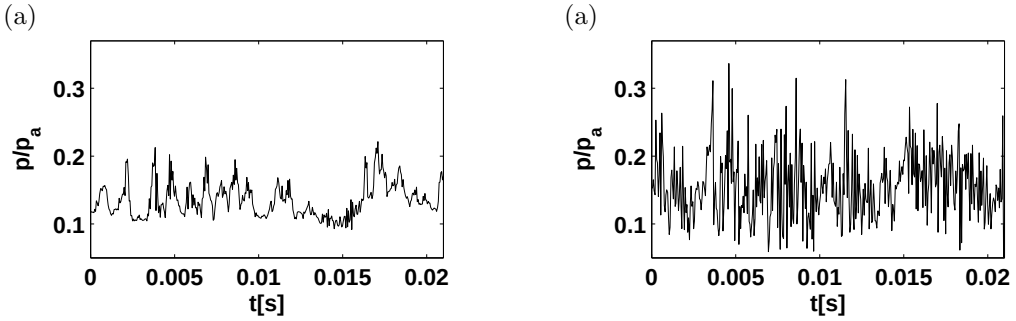

Figure 13. Pressure signal recorded in (a) the reattachement region ($x = H/2$) and in (b) the separated flow region further downstream at $x = 2H$.

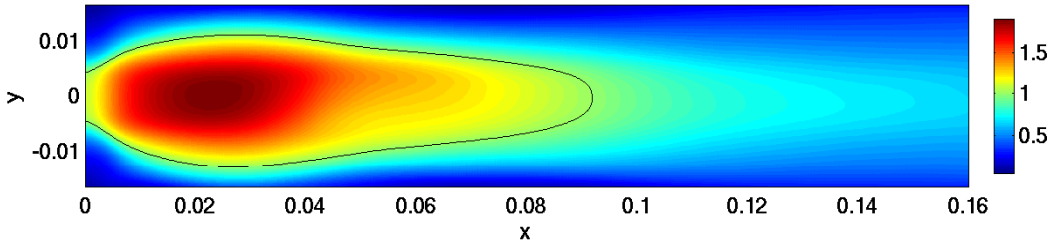

Figure 14. Mean Mach number in the duct: the solid line stands for $M = 1$.

downstream of an abrupt increase in duct cross-section. Mitteilung aus dem Max-Planck-Institut fuer Stroemungsforschung und der Aerodynamischen Versuchsanstalt, **65** (1978), 1-172.

[3]Lafon P., Devos J. P. *Numerical prediction of instabilities in transonic internal flows using an Euler TVD code.* AAIA Paper, (1993) 1993-72.

[4]Visbal M.R., Gaitonde D.V. *On the use of higher-order finite-difference schemes on curvilinear and deforming meshes.* Journal of Computational Physics, **181** (2002), 155-185.

[5]Marsden O., Bogey C. and Bailly C. *High-order curvilinear simulations of flows around non-Cartesian bodies.* Journal of Computational Acoustics, **13**(4) (2005), 732-748.

[6]Bogey C., Bailly C. and Juvé D. *A family of low dispersive and low dissipative schemes for Large Eddy simulations and for sound propagation.* Journal of Computational Physics, **194** (2004), 194-214.

[7]Berland J., Bogey C. and Bailly C. *Optimized explicit schemes: matching and boundary schemes and 4th- order Runge-Kutta algorithm.* AIAA Paper, 2004-2814.

[8]Kim J.W., Lee D.J. *Adaptive non-linear artificial dissipation model for Computational Aeroacoustics.* AIAA Journal, **39** (2001), 810-818.

[9]Hardin J.C., Ristorcelli J.R. and Tam C.K.W. *Workshop on benchmark problems in computational aeroacoustic.* NASA, ICASE, (1995).

[10]Landau L., Lifchitz E. *Mécanique des fluides.* Pergamon Press, 2nd edition (1987).

[11]Tam C.K.W., Dong Z. *Radiation and outflow boundary conditions for direct computation of acoustic and flow disturbances in a nonuniform mean flow.* Journal of Computational Acoustics, **4** (1996),175-201.

[12]Jungowski W.M. *Investigation of flow pattern, boundary conditions and oscillation mechanism in a compressible flow through sudden enlargement of a duct.* Warsaw Techn. Univ. Publ., **3** (1968).